Setting and hardening process of a wollastonite-based brushite cement

Priscillia Laniesse, Céline Cau Dit Coumes, Arnaud Poulesquen, Agathe Bourchy, Adel Mesbah, Gwenn Le Saout, Philippe Gaveau

Setting and hardening process of a wollastonite-based brushite cement

Priscillia Laniesse[a], Céline Cau Dit Coumes[a,*], Arnaud Poulesquen[a], Agathe Bourchy[a], Adel Mesbah[b], Gwenn Le Saout[c], Philippe Gaveau[d]

[a] CEA, DEN, DE2D, SEAD, F-30207 Bagnols-sur-Cèze cedex, France
[b] ICSM, UMR 5257 CNRS - CEA – ENSCM, Université de Montpellier, Site de Marcoule - Bat 426, BP 17171, 30207 Bagnols/Cèze, France
[c] IMT Mines Alès, C2MA, 30319 Alès, France
[d] Institut Charles Gerhardt de Montpellier, UMR 5253, CNRS UM ENSCM, Montpellier 34095, France

ABSTRACT

Wollastonite-based brushite cements are used for refractory material applications, but they may also offer prospects for the solidification/stabilization of hazardous waste. These binders are formed by the reaction of wollastonite with an orthophosphoric acid solution containing borax and metallic cations (Al^{3+}, Zn^{2+}). This work provides new insights into their setting and hardening process using a panel of characterization techniques (XRD, NMR, rheology...). A multi-step hydration process is evidenced by the formation of several products: amorphous silica, monocalcium phosphate monohydrate ($Ca(H_2PO_4)_2{\cdot}H_2O$ or MCPM), that precipitates transiently during the first stage of hydration, and brushite ($CaHPO_4{\cdot}2H_2O$) that crystallizes at higher pH (≥3). In addition, an amorphous phosphate phase containing aluminum, calcium and zinc massively precipitates at the beginning of hydration, and gets richer in calcium as hydration progresses. Setting of the cement paste occurs when brushite starts to form. The successive formation of MCPM and brushite is well predicted by thermodynamic modelling.

Keywords:
Hydration (A)
Microstructure (B)
Hydration products (B)
Chemically bonded ceramics (D)
Thermodynamic calculations (B)

1. Introduction

Calcium phosphate cements are usually composed of one or several phases containing calcium and phosphates, to which other calcic compounds as calcium hydroxide or calcium carbonate can possibly be added as well as additives to control the setting and the properties of the hardened matrix [1 3]. Mixed with aqueous solutions, they can yield different end products, such as stoichiometric or calcium deficient hydroxyapatite, calcium octaphosphate ($Ca_8(H_2PO_4)_6{\cdot}5H_2O$) or brushite ($CaHPO_4{\cdot}2H_2O$), by an acid base or hydrolysis reaction [4]. The main applications of phosphate cements are in the dentistry and medicine area since they form a product with a similar chemical composition to bones and teeth [5 11]. Regarding apatite cements ($Ca_5(PO_4)_2OH$), certain properties are also of interest for applications concerning radioactive wastes conditioning, such as their structural flexibility, high temperature stability, very low solubility in slightly acidic, neutral, or alkaline aqueous media and irradiation stability [12]. However, a limitation of these binders for use on a large scale is the cost of some of the reactants prepared at high temperature (tetracalcium and tricalcium phosphates).

A less expensive calcium phosphate binder can be prepared from wollastonite ($CaSiO_3$), a natural calcium meta silicate, and phosphoric acid (H_3PO_4), as firstly described by Semler [13,14]. The reaction starts in very acidic medium (pH ~ 1), but the pH increases rapidly to reach equilibrium at a value close to 6 [15]. For Ca/P molar ratios between 1 and 2.56, a calcium phosphate (brushite ($CaHPO_4{\cdot}2H_2O$)) and amorphous silica are formed according to equation (Eq. (1)) [15,16].

$$CaSiO_3 + H_3PO_4 + (1 + x)\,H_2O \rightarrow SiO_2{\cdot}xH_2O + CaHPO_4{\cdot}2H_2O \quad (1)$$

However, wollastonite based binders are highly reactive and can exhibit flash set as well as excessive heat output [15] and need to be strongly retarded, for instance by an addition of boron species, such as borax or boric acid [14].

Wollastonite based brushite cements have found applications for refractory materials as they exhibit very good thermal resistance after hydrothermal post curing [17]. Textile reinforced cementitious composites have been successfully designed for applications requiring high load bearing capacity, good fire resistance and lightweight construction [18]. Due to very different cement chemistries, some retarders of Portland cement hydration such as heavy metals may be much less influent on the setting and hardening process of wollastonite based binders. For instance, lead oxide can be incorporated up to 50% by weight of cement (wollastonite) without notable degradation of the mechanical and thermal properties [19]. The resulting composites have

* Corresponding author.
E-mail address: celine.cau-dit-coumes@cea.fr (C. Cau Dit Coumes).

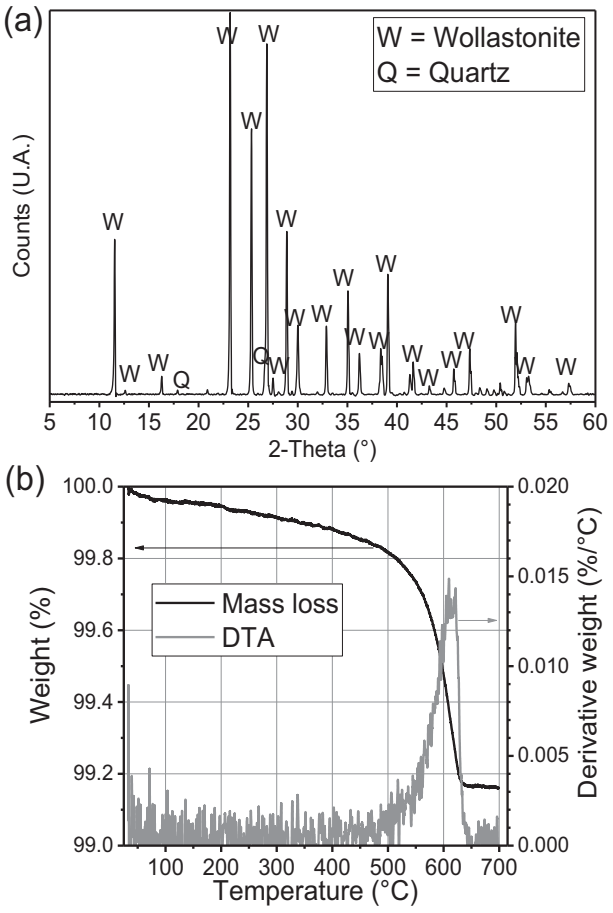

Fig. 1. Mineralogical characterization of the cement powder by X-ray diffraction (a) and thermogravimetry analysis (b).

potential for radiation shielding applications. Good adhesion properties with wood products, ceramics and concrete have also been recently reported, which opens up their spectrum of applications [20].

Most studies on wollastonite based binders have been focused on the characterization of the final products [15,20], on the associated microstructure [15] and on the functional properties of the resulting materials [17,21,22]. This work aims at giving a new insight into the setting and hardening process of such binders, by characterizing the evolution of both the liquid and solid phases with ongoing hydration.

2. Experimental

2.1. Materials and specimen preparation

The wollastonite based binder was provided by Sulitec. It was a two component system, consisting of a calcium silicate powder and of a phosphoric acid based solution. The powder mainly comprised wollastonite, and traces of calcite and quartz as shown by X ray diffraction and thermogravimetric analysis (Fig. 1). Calcite resulted from carbonation of metastable wollastonite when exposed to air.

Based on the weight loss recorded at 654 °C (decarbonation of $CaCO_3$) by thermogravimetric analysis, the proportion of calcite was assessed to be 1.6 ± 0.1 wt%. The particle size distribution of the powder, determined by laser granulometry, ranged between 0.5 μm and 135 μm (d_{10} = 2.8 μm, d_{50} = 15.2 μm, d_{90} = 48.3 μm). During industrial crushing, wollastonite breaks into lath or needle shaped particles because of its cleavage properties. This tendency is measured by the ratio of the length to diameter of the particles. The average aspect ratio, measured on SEM images (characterization of 100 particles), was close to 4:1, which is rather small as compared to other commercial wollastonites.

The mixing solution was a phosphoric acid solution ([P] = 9.3 mol/L), containing metal cations ($[Al^{3+}]$ = 1.3 mol/L, $[Zn^{2+}]$ = 1.3 mol/L) and borax ($[Na_2B_4O_7]$ = 0.15 mol/L) as a retarding agent. The weight ratio of the mixing solution to the cement powder was fixed to 1.25 in all samples, resulting in a Ca/P molar ratio of 1.2. Mixing was performed during 5 min using a laboratory mixer equipped with an anchor stirrer and rotating at 250 rpm. Paste samples were cast into airtight polypropylene boxes (20 mL of paste per box) and cured at 25 ± 1 °C for a period of time ranging from 30 min to 48 h, before being characterized to determine their mineralogy and microstructure (Section 2.2.2). The cement hydration process was also investigated using a panel of complementary techniques, as described in Section 2.2.1.

2.2. Characterization techniques

2.2.1. Characterization of cement hydration

Hydration of the cement pastes was investigated using a TAM AIR conduction microcalorimeter under isothermal conditions at 25 °C. Calorific capacities of solution and cement were respectively taken equal to 3.76 and 0.75 J/°C/g. Mixing of the dry cement and solution was performed outside the calorimeter. About 2 g of cement paste was cast in a glass ampoule and introduced in the calorimeter. The heat flow was recorded versus time and compared to that of a sample maintained at 25 °C and consisting of water, the volume of which being adjusted to get the same calorific capacity as the paste sample.

The Vicat setting time was measured according to European standard EN 196 3. The needle was on a 300 g moveable rod and had a diameter of 1 mm ± 0.05 mm. A sample of fresh cement paste was cast in a frustum 40 mm in height. Initial setting time was considered as the time when the needle penetration was 39 mm ± 0.5 mm. The final setting time corresponded to < 0.5 mm penetration. To avoid any desiccation of the paste during setting, a layer of Vaseline oil was poured on the material before starting the experiment. Penetration was then measured every 30 min. Oil was used instead of water since it was observed that the presence of curing water retarded cement setting. This delay was likely due to the dilution of the acidic mixing solution and its pH increase. In the presence of oil, the samples exhibited the same setting time as the pastes cured in air tight polypropylene boxes at 25 °C.

In addition, the viscoelastic properties and electrical conductivity of the paste samples were simultaneously monitored with ongoing hydration using a specifically designed device [23]. It comprised a cylindrically shaped Plexiglas cell (inner radius of 15 mm, total volume of 70 mL) with two annular stainless steel electrodes, which was filled with the cement paste. The cell was thermostated at 25 °C by circulation of cooling water in a double envelope. It was connected to the EC channel of an electrochemistry meter (Consort C 861) with a BNC cable. A specific data acquisition software (Consort Dis Data) was used to collect conductivity measurements. The conductivity cell was calibrated using a 12.888 mS/cm standardized KCl solution at 25 °C. Evolution of the viscoelastic properties of the paste was followed by dynamic mode rheometry using a strain driven controlled stress rheometer (AR G2 TA Instrument, USA). A sinusoidal shear strain (γ) was applied to the cement paste at constant frequency (ω). The resulting stress (τ) was measured by the intermediary of the torque and was also sinusoidal with a δ phase lag with respect to the applied strain.

$$\gamma = \gamma_0 e^{i\omega t} \quad (2)$$

$$\tau = \tau_0 ei(\omega t + \delta) \quad (3)$$

The ratio between the stress and the shear strain is equal to the complex shear modulus (G*) and is defined by:

$$G^* = G' + iG'' \quad (4)$$

with G′ the shear storage modulus, and G″ the shear loss modulus.

A strain sweep experiment was carried out at a frequency of 1 rad/s on paste samples after increasing hydration times (just after mixing, 10 h, 24 h and 30 h): the viscoelasticity plateau ended at a shear strain of 10^{-3}, in all cases. In order to stay within the linear viscoelasticity domain of the materials, and thus to avoid destructive measurement, the dynamic mode rheometry experiments were performed using a 10^{-4} shear strain and a 1 rad/s frequency. A specific vane geometry (stainless steel, radius of 20 mm, length of 3 cm) was used to perform all the experiments. This geometry was selected for two reasons:

1. the same tool could be used to mix the sample to get a better homogeneity just before the rheometric characterization, so that all the materials had the same history before beginning the experiment,
2. it was much less sensitive to segregation than the classical parallel plate geometry.

Moreover, it has been shown on several different types of materials that this geometry gives the same rheological information or signature than the conventional parallel plate geometry [24]. The vane geometry was calibrated with standard oil (S6300, 1.41 Pa·s, at 25 °C, PSL), as well as with a non Newtonian fluid (water + 0.5% Xanthan) [25].

The shrinkage cone (Schleibinger Geräte) method was used to measure the evolution of the apparent volume of the cement paste at early age. The device was initially developed by the German Cement Works Association for measuring the autogenous shrinkage of concrete [26,27]. The device was described by Lafond et al. [28]. It consisted of a laser vertically pointed at the surface of a cone shaped sample thermostated at 25 °C. The cone geometry (10 cm height by 11.5 cm diameter in the opening) of the sample ensured that the change in height corresponded to the linear length change of the material as long as it was fluid and also after solidification since deformation was considered as uniform. After pouring the sample in the cone, its surface was covered with a plastic sheet equipped with a reflector to avoid desiccation. The jar was then placed underneath the laser, and the distance variation between the reflector and the laser was recorded every minute. The measurement range was 5 mm, with a resolution of 0.1 µm. The volume variation normalized by the initial volume is given in Eq. (5), with V_0 and V the initial volume and the volume at time t respectively, h_0 the initial height, and Δh the height variation given by the device.

$$\frac{\Delta V}{V_0} = \frac{V - V_0}{V_0} = \left(\frac{h_0 + \Delta h}{h_0}\right)^3 - 1 \tag{5}$$

2.2.2. Characterization of the microstructure and mineralogy

Cement hydration was stopped after fixed periods of time by successively immersing the crushed paste into isopropanol, filtrating the suspension and drying it in an oven at 38 °C for 4 h. Preliminary tests showed that two samples dried at 38 °C for 24 h or at room temperature during several days exhibited the same mineralogy.

Thermogravimetric analyses were carried out in 30 µL crucibles under N_2 atmosphere (gas flow set at 50 mL/min) using a METTLER TOLEDO TGA/DSC 3+ instrument at 2 °C/min up to 700 °C. The curves were corrected from buoyancy effects (caused by the density of the surrounding gas decreasing on heating) by performing a blank subtraction.

Crystallized phases were qualitatively analysed by powder X ray diffraction with the Bragg Brentano geometry (PanAlytical X'pert Pro, copper anode, $\lambda_{K\alpha 1}$ = 1.5418 Å, scanning from 2θ = 5° to 70° in 0.017° steps, for a total counting time of 42 min) on pastes ground by hand to a particle size < 80 µm. To get a quantitative evolution of the phases during the hydration process, samples aged from 30 min to 7 days were analysed using the Debye Scherer configuration (transmission mode). They were introduced in Lindeman tubes (Φ = 0.7 mm) and mounted on a spinning goniometric head during measurement to reduce the preferred orientation effect. Data were recorded by using copper radiation (λ = 1.5418 Å) at room temperature in the 2 θ range 5 120° with a step size of 0.017° for a total counting time of 6 h. Powders were finely ground at a particle size below 80 µm with 10 wt% silicon used as an internal standard for quantitative analysis. Fullproof suite software was used for the quantitative analysis of the different phases with the Rietveld method [29]. Rietveld refinements allowed to determine the weight fractions of each crystalline phase and of total amorphous.

The reactions occurring during hydration not only consumed water, but also ions from the solution (phosphate, aluminum, zinc, boron, sodium). On the contrary to a Portland cement paste, the weight of solid at a given hydration time could not be simply calculated by adding to the initial mass of solid the amount of bound water determined by TGA. Therefore, a quantitative elemental analysis was necessary to determine the mass of solid, and thus to assess that of residual wollastonite and precipitated products. To do so, two types of total digestions were carried out.

1. Liquid digestion: about 10 g of sample were digested in 20 mL of aqua regia (3.2 mol/L of HNO_3 and 9.6 mol/L of HCl). The digestion took 1 h to complete. Since aqua regia partially decomposed during this period, the remaining volume at the end of the digestion was measured. Then, 1 mL aliquots were sampled and diluted in 9 mL of 2 wt% HNO_3 solution. This method made it possible to analyse all the cement elements (Al, Zn, P, Na, B) excepting Si for which the results were poorly repeatable.
2. Solid digestion: the solid digestion was carried out in lithium metaborate to quantify Ca, Al, Zn, P, Na and Si. The powder was fused at 950 °C with a sample to metaborate ratio equal to 0.25. After digestion, the paste was solubilized in a 20 wt% HCl solution.

In both cases, the resulting samples were analysed by ICP AES and the weight fractions of Al, Zn, P, Na, Si and B in the solid could be determined. Analysis of the liquid phase by ICP AES up to 7 h of hydration (see below in Section 2.2.3) showed that the concentration of dissolved silica was negligible (< 2 mmol/L). It was thus postulated that silica was only present in the solid phase (as amorphous silica resulting from incongruent dissolution of wollastonite and as a component of wollastonite). According to mass conservation equation (Eq. (6)), the total mass of silica in the solid phase ($m(Si)_{sol}$) was thus assumed to be equal to the initial mass of silica ($m(Si)_{ini}$).

$$m(Si)_{ini} = m(Si)_{liq.} + m(Si)_{sol.} \tag{6}$$

with $m(Si)_{liq}$ the mass of Si in the liquid phase, which was neglected.

Then, the total mass of solid phases at time t ($m(Sol.)_t$) was calculated using Eq. (7)).

$$m(Sol.)_t = \frac{m(Si)_{sol,t}}{wt.\ \%(Si)_{sol,t}} = \frac{m(Si)_{ini}}{wt.\ \%(Si)_{sol,t}} \tag{7}$$

with $m(Si)_{sol,t}$ the total mass of Si in the solid at time t, $wt\%(Si)_{sol,t}$ the weight fraction of Si in the solid at time t determined by ICP AES and $m(SiO_2)_{ini}$ the initial mass of SiO_2 (present as a component of wollastonite).

Knowing the mass of solid over hydration time, the mass of each phase was calculated using the results from Rietveld analysis. Then, the mass of amorphous silica at time t ($m(SiO_2(am))_t$) was inferred from mass balance equation (Eq. (8)).

$$m(SiO_2(am))_t = m(SiO_2)_{ini} - m(CaSiO_3)_t \times \frac{M(SiO_2)}{M(CaSiO_3)} \tag{8}$$

with $m(CaSiO_3)_t$ the mass of wollastonite at time t, $M(SiO_2)$ and $M(CaSiO_3)$ the molar weights of silica and wollastonite respectively.

Finally, the weights of all the other phases being assessed, the amounts of aluminum, calcium, phosphorus and zinc in the amorphous phase were calculated using mass conservation.

The microstructure evolution was observed by Scanning Electron

Table 1
Calcium phosphate minerals added to the Chess Database.

	Species	Formation reaction	Log K (T = 25 °C, P = 1 bar) [4]
Aqueous	$CaH_2PO_4^+$	$Ca^{2+} + HPO_4^{2} + H^+ \rightarrow CaH_2PO_4^+$	8.712
	$CaHPO_4$ (aq)	$Ca^{2+} + HPO_4^{2} \rightarrow CaHPO_4$ (aq)	2.74
	$CaPO_4$	$Ca^{2+} + HPO_4^{2} \rightarrow CaPO_4$ (aq) + H^+	5.8618
Minerals	MCPM ($Ca(H_2PO_4)_2{\cdot}H_2O$)	$Ca^{2+} + 2HPO_4^{2} + 2\ H^+ + H_2O \rightarrow Ca(H_2PO_4)_2{\cdot}H_2O$	17.38
	Brushite ($CaHPO_4{\cdot}2H_2O$)	$Ca^{2+} + HPO_4^{2} + 2\ H_2O \rightarrow CaHPO_4{\cdot}2H_2O$	6.59
	OCP ($Ca_8(H_2PO_4)_6{\cdot}5H_2O$)	$8\ Ca^{2+} + 6\ HPO_4^{2} + 5\ H_2O \rightarrow Ca_8(HPO_4)_2(PO_4)_4{\cdot}5H_2O + 4H^+$	19.8428
	Hydroxyapatite ($Ca_5(PO_4)_3(OH)$)	$5\ Ca^{2+} + 3\ HPO_4^{2} + H_2O \rightarrow Ca_5(PO_4)_3(OH) + 4H^+$	7.5595
	CDHA ($Ca_9(HPO_4)(PO_4)_5(OH)$)	$9\ Ca^{2+} + 6HPO_4^{2} + H_2O \rightarrow Ca_9(HPO_4)(PO_4)_5(OH) + 6\ H^+$	12.7859
	$Ca_4H(PO_4)_3{\cdot}2.5H_2O$	$4\ Ca^{2+} + 3\ HPO_4^{2} + 2.5\ H_2O \rightarrow Ca_4H(PO_4)_3{\cdot}2.5H_2O + 2H^+$	9.8062
	$Ca_4H(PO_4)_3{\cdot}3H_2O$	$4\ Ca^{2+} + 3HPO_4^{2} + 3\ H_2O \rightarrow Ca_4H(PO_4)_3{\cdot}3H_2O + 2H^+$	11.4962

Microscopy (FEI Inspect S50, high vacuum mode, acceleration voltage of 15 kV, current intensity of 50 nA, working distance of 9.7 mm) on sample fractures and polished sections at different ages. The polished sections were prepared by impregnating cement pastes (in which hydration was stopped) with an epoxy resin (EPO TEK 301) under vacuum. The samples were then polished using several diamond grades (down to 1 μm) and carbon coated using a carbon evaporator (Quorum Q150TE). The Ca/P, Al/P and Zn/P ratios in the hydrates were determined by X ray microanalysis on polished cross sections (high vacuum mode, Bruker X flash SDD detector (10 mm^2) calibrated on jadeite for Na, alumina for Al, zinc metal for Zn, GaP for P and wollastonite for Si and Ca, statistics on 20 to 30 measurement points).

Some paste samples were characterized using ^{31}P and ^{27}Al MAS NMR. Experiments were carried out on a VARIAN VNMRS 600 MHz (14.1 T) spectrometer using a 3.2 mm T3 MAS (Magic Angle Spinning) probe with ZrO_2 rotors spun at 20 kHz. ^{31}P NMR MAS spectra were recorded at 242.81 MHz using presaturation followed by a single pulse with 90° pulses of 3 μs, recycle delay of 240 s, 16 transients and spinal ^1H decoupling during acquisition. The recycle delay was set to 240 s, in order to respect the relaxation times T_1 of the amorphous species present in the sample. However, phosphate crystalline species have extremely long relaxation delay. Therefore, the relative contribution of crystalline phases in regards to amorphous species was underestimated. Chemical shifts were referenced to external K_2HPO_4 at 4.1 ppm (used as a secondary reference). ^{27}Al NMR MAS spectra were acquired at 156.30 MHz using single pulse experiments with a 15° pulse of 1 μs, recycle delay of 1 s, 4096 transients and CW (continuous wave) ^1H decoupling during acquisition. Chemical shift were referenced to external $Al(NO_3)_3$ solution (0 ppm).

2.2.3. Characterization of the interstitial solution

During the first 7 h of hydration, the pore solution of the paste samples could be extracted by compaction of about 20 g samples with a RETSCH PP25 mechanical press at a pressure of 34 MPa. The elemental composition of the interstitial solution was determined using ICP AES (Thermo Fisher ICAP 6300 Duo) previously calibrated with external standards (solutions of Al, B, Ca, Na, P, Si and Zn) and matrix reconstitution. Samples were diluted in a 2 wt% nitric acid solution before their analysis.

As the solutions were initially very acidic, their pH could not be measured directly with a pH electrode. Therefore, their acidity function H_0 was determined. This function was first developed by Hammett [30] and provides a quantitative measure of acidity derived from ionization equilibria of an indicator behaving in the Brönsted Lowry sense.

$$BH^+ = B + H^+$$

The acidity function is defined by Eq. (9).

$$H_0 = pK_{BH} + \log\,(C_B/C_{BH}) \quad (9)$$

The ratio between the de protonated and protonated forms can be determined by several techniques (vapor pressure [31], electrochemical [32] and spectroscopic [33 36] measurements). In this work, the acidity function was determined using UV visible spectroscopy. The 4 chloro 2 nitroaniline was chosen as the acidity indicator for two reasons: its pK_{BH} value of −0.89 at 19 °C falls within the range of interest and it has already been used for acidity function measurement of phosphoric acid solutions [37]. The indicator concentration was taken equal to 5.10^{-5} mol/L, the spectra were recorded 30 min after mixing (to reach equilibrium) and the absorption values were measured at 432 nm using Genesis 10S UV Vis (Thermo Scientific) spectrophotometer. The acidity function was then calculated using Eq. (10), where A_x^{432} was the absorbance of solution X at 432 nm and A_0^{432} was the absorbance of the fully deprotonated indicator in an aqueous solution at 432 nm.

$$H_0 = -0.89 + \log\,(A^{432}{}_x/(A^{432}{}_0 - A^{432}{}_x)) \quad (10)$$

2.3. Thermodynamic modelling

Experiments were supported by thermodynamic equilibrium modelling in order to predict the evolution of the mineralogy of the cement paste with ongoing hydration. Thermodynamic calculations were carried out using CHESS software which works by minimizing the free energy of a predefined system [38].

The quality of modelling directly depends on the quality and completeness of the underlying database [39]. The Chess database was enriched by adding new calcium phosphate species relevant to the investigated system. They are summarized in Table 1, together with their formation constants. Because of the rather high ionic strength of the pore solution, the activities of the dissolved species could not be simply assessed by their concentrations. Initially, the ionic strength of the mixing solution was extremely high. According to Cherif et al.[40], a concentrated phosphoric acid solution (9 mol/L) contains 5 mol/L H^+, 1.5 mol/L $H_2PO_4^-$ and 3.5 mol/L $H_5P_2O_8^-$. However, when the products started to precipitate, the ionic strength dropped below 0.75 mol/L. The B dot model [41] was thus used to take into account electrostatic and steric interactions. The model, which is an extension of the Debye Hückel equation, is considered reasonably accurate in predicting the activities of Na^+ and Cl^- ions to concentrations as large as several mol/kg, and of other species to ionic strengths up to 0.3 to 1 mol/kg.

3. Results and discussion

3.1. Evolution of the acidity of the pore solution

The evolution of the acidity function measured up to 7 h of hydration is given in Fig. 2. H_0 values increased during this period, meaning that the solution became less acidic over time. This evolution could be explained by the progressive dissolution of wollastonite which consumed protons from the solution (Eq. (11)).

$$CaSiO_3 + 2H^+ + xH_2O \rightarrow Ca^{2+} + SiO_2{\cdot}(x+1)H_2O\ (am) \quad (11)$$

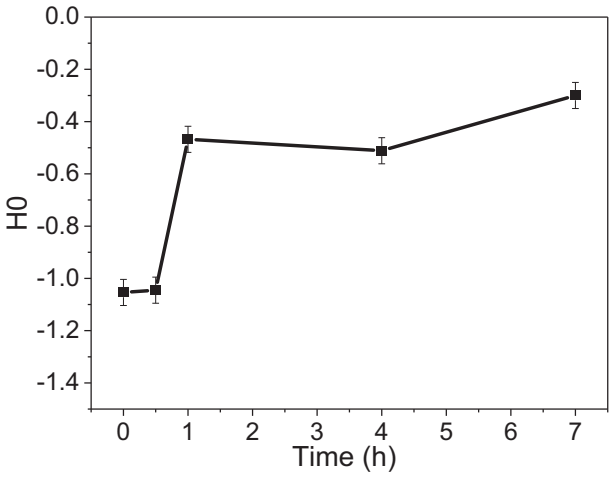

Fig. 2. Evolution of the acidity function of the interstitial solution up to 7 h of hydration.

3.2. Evolution of the cement paste over the first 48 h

The evolution of the viscoelastic parameters, heat flow and elec trical conductivity in the cement paste during the first 48 h after mixing are shown in Fig. 3.

Four stages could be defined from the rheometric measurements.

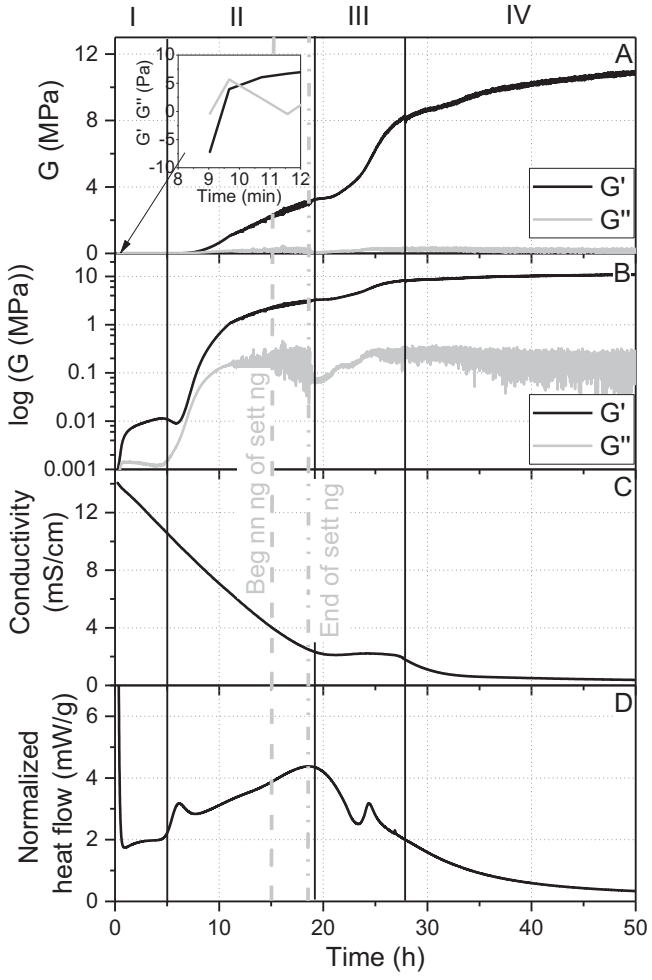

Fig. 3. Evolution of the viscoelastic parameters (A and B), electrical conductivity (C) and heat flow (D) with ongoing hydration.

Table 2
Enthalpy of reaction occurring during hydration of wollastonite [54,55].

Type of reaction	Balance equation	Enthalpy of reaction (kJ/mol)
Wollastonite dissolution	$CaSiO_3 + 2H^+ \rightarrow Ca^{2+} + SiO_2 + H_2O$	96.46
MCPM precipitation	$Ca^{2+} + 2H_3PO_4 + H_2O \rightarrow Ca(H_2PO_4)_2{\cdot}H_2O + 2H^+$	4.36
Brushite precipitation	$Ca^{2+} + H_3PO_4 + 2H_2O \rightarrow CaHPO_4{\cdot}2H_2O + 2H^+$	0.77
Conversion MCPM → Brushite	$Ca(H_2PO_4)_2{\cdot}H_2O + H_2O \rightarrow CaHPO_4{\cdot}2H_2O + H_3PO_4$	3,59

3.2.1. Stage 1: from 0 to 5 h

From 0 to 5 h, the storage and shear loss modulus exhibited a first increase of rather small magnitude, and reached a plateau. Initially, the shear loss modulus was higher than the storage modulus, meaning that the paste had a liquid like behaviour. However, the storage modulus increased rapidly and exceeded the shear loss modulus only a few minutes after the beginning of the experiment. This indicated the transformation of a dispersed system of cement grains into a network showing the characteristics of a solid. Note however that, if the paste exhibited some kind of cohesion shortly after mixing, it remained flowable by applying a small mechanical solicitation. During this period, the electrical conductivity began to decrease, which could be explained by a decrease in the acidity of the interstitial solution (see Section 3.1) and by the precipitation of the first hydrates. From a thermal point of view, the first minutes were characterized by heat production which resulted from several factors: start of dissolution of wollastonite (Table 2), but also, and mainly, introduction of the ex ternally prepared sample in the calorimetric chamber, which biased the signal for 30 to 45 min. The powder X ray diffraction patterns showed the precipitation of small amounts of well crystallized MonoCalcium Phosphate Monohydrate (MCPM: $Ca(H_2PO_4)_2{\cdot}H_2O$). The presence of amorphous phases was also pointed out by Rietveld quantification using the internal standard method (silicon). One expected product according to Mosselmans et al. [15] is amorphous silica. However the sole precipitation of amorphous silica could not explain the amount of amorphous phase calculated by Rietveld analysis (40 g of amorphous phase, whereas only 5 g of wollastonite was consumed at 4 h, meaning that 2.6 g of silica at most could have been produced). Therefore, an additional amorphous product was present. Mass balance calculations showed that it contained aluminum, phosphate, zinc and calcium (Fig. 4 B). According to the calculated phase evolution, only small amounts of wollastonite dissolved during this stage, leading to small amounts of MCPM and silica (Fig. 4 B). The main product was thus the phosphate containing amorphous phase. The observation of a polished section of a 30 min old sample confirmed the presence of a phosphate rich product containing aluminum and zinc (shown in blue in Fig. 5), which could correspond to the amorphous phase. According to EDS analyses (Fig. 6), its average Ca/P, Al/P and Zn/P were respectively 0.13 ± 0.06, 0.28 ± 0.05 and 0.22 ± 0.04.

The early precipitation of an amorphous product has already been reported for zinc phosphate dental cement [42], but has never been fully characterized. To obtain more information, ^{31}P and ^{27}Al NMR spectra were acquired on the 30 min old sample (Fig. 7). The ^{31}P NMR spectrum showed the presence of MCPM (peaks at 0.1 and −4.3 ppm assigned to Q_0 units where Q is the PO_4 tetrahedral units and n the number of bridging oxygen per tetrahedron [43]), but other contribu tions in the Q_0 and possibly in the Q_1 range were also noticed at −1.3, −6.7 and −12.5 ppm. In addition, the ^{27}Al spectrum showed the pre sence of a peak (at −13.3 ppm) characteristic of octahedral aluminum forming Al $(OP)_6$ units [44]. Also, ^{27}Al spectrum showed the presence of two other minor contributions (5% each) at 7.9 and 57.9 ppm, which

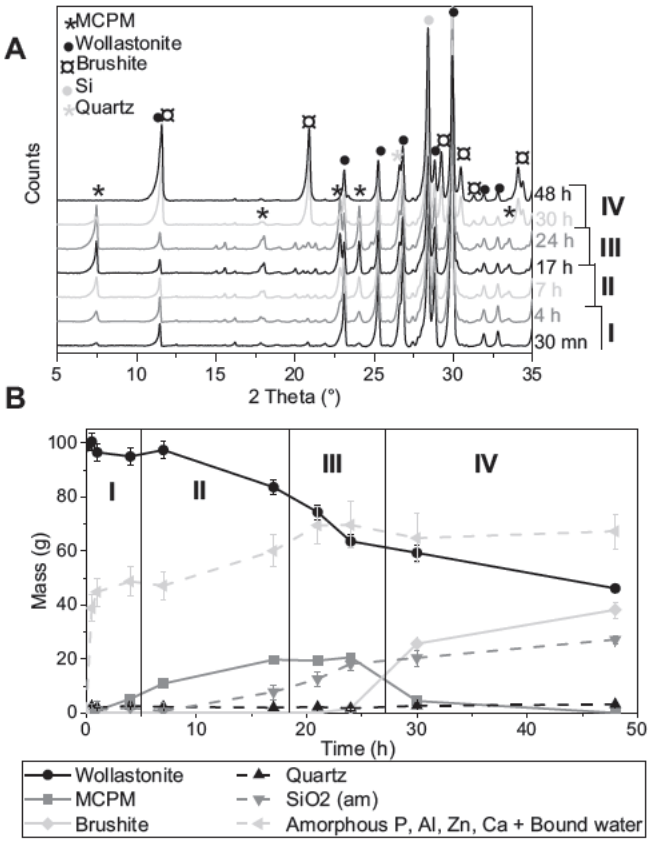

Fig. 4. Evolution of the phase assemblage with ongoing hydration: (a) X-ray diffraction patterns; (b) phase evolution assessed from Rietveld and elemental analysis as well as mass balance calculations.

might correspond to AlO_6 and AlO_4 respectively. Therefore, ^{27}Al and ^{31}P NMR experiments also suggested the formation of an alumino phosphate phase at the beginning of hydration.

According to Rietveld analysis and mass balance calculations, this phase exhibited the following composition: $(ZnO)_{0.40 \pm 0.06}(Al_2O_3)_{0.24 \pm 0.03}(P_2O_5)_{1.0 \pm 0.1}{\cdot}xH_2O$. The Zn/P and Al/P ratio were in rather good agreement with those determined by EDS analysis. However, the calculated composition was free of calcium whereas this element was detected in small amount by EDS analysis (Ca/P molar ratio = 0.11 ± 0.02). Two assumptions were considered to explain these contradictory results: (*i*) the amorphous phase actually contained small amounts of calcium which were not evidenced by the mass bal ance calculation due to experimental uncertainties, (*ii*) the calcium detected by EDS analysis was due to intermixing at the submicronic level of the amorphous phase with other calcium containing minerals (wollastonite, MCPM).

Finally, the 30 min old sample was characterized by thermogravi metric analysis (Fig. 8). It showed a much higher weight loss (7 wt%) than the initial cement powder, with two thermal events: the first one from 55 to 130 °C and the second at 148 °C. This weight loss largely exceeded that calculated assuming the dehydration of the crystallized phases (0.07 wt%). Different explanations could be postulated to ex plain these two weight losses:

the weight loss at 55 °C might be partially assigned to evaporation of residual isopropanol used for stopping cement hydration;
hydrated amorphous silica dehydrated between 45 and 100 °C and 135 150 °C, in agreement with previous results reported for hy drated nanosilica [45];
the alumino phosphate amorphous phase could also be hydrated and loose water within these ranges of temperature.

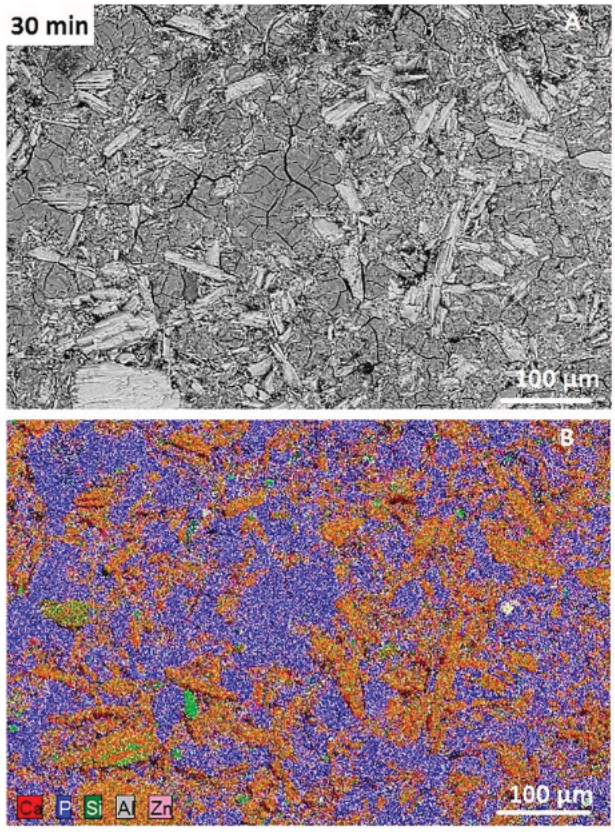

Fig. 5. SEM observation of the polished section of a 30 min-old sample. Top: BSE image; Bottom: elemental mapping (Ca, Al, P, Si, Zn).

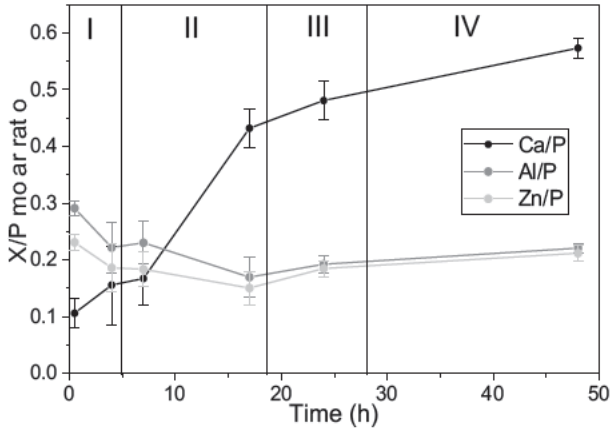

Fig. 6. Evolution of the Ca/P, Al/P and Zn/P molar ratios of the amorphous phosphate phase.

At 30 min, the water content measured by TGA was equal to 7.3% corresponding to 10.4 g of water in the solid phase. If we assume that amorphous silica was the only hydrated product ($SiO_2{\cdot}xH_2O$), the water to silica ratio at this stage of hydration should be as high as 16.7, which seems unlikely [46]. Therefore, the alumino phosphate amor phous phase was probably also hydrated.

3.2.2. Stage 2: from 5 h to 18 h

From 5 h to 18 h, the storage modulus and the shear loss modulus exhibited a second increase. The storage modulus largely exceeded the shear loss modulus, by more than one decade, at the end of this stage. The paste thus consolidated progressively and the beginning of setting measured using the Vicat needle occurred at 15 h. The analysis of the

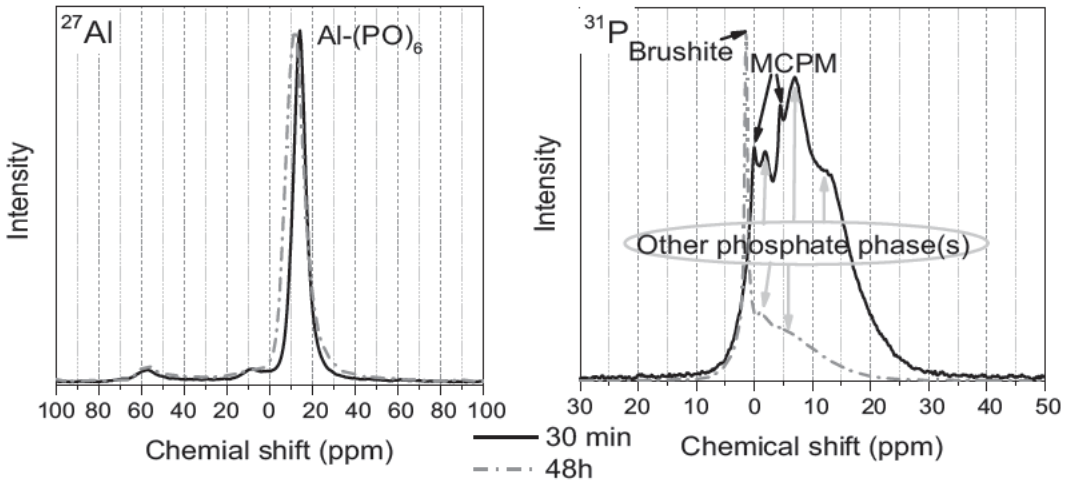

Fig. 7. ^{27}Al and ^{31}P MAS NMR spectra of the 30 min and 48 h-old samples.

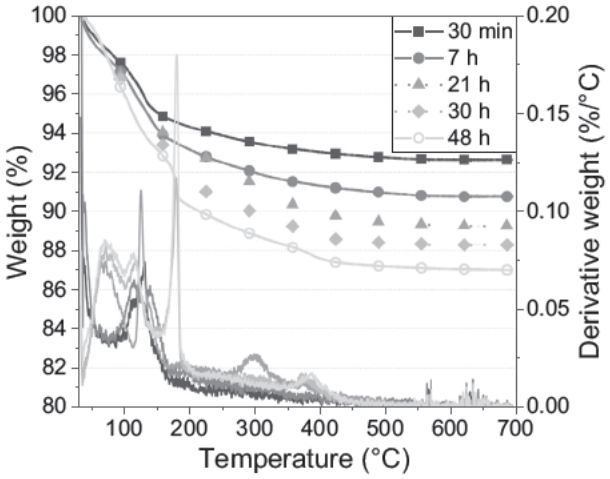

Fig. 8. Thermograms of paste samples aged from 30 min to 48 h.

phase assemblage (Fig. 4) showed a faster consumption of wollastonite, accompanied by the increased precipitation of MCPM and amorphous silica. The amount of the amorphous aluminum phosphate phase continued to increase, but much less rapidly than in stage I. The formation of MCPM is only slightly exothermic (Table 2). However, the consumption of calcium ions from the solution accelerated the exothermic dissolution of wollastonite (Table 2). As a result, the heat flow exhibited a peak at 6 h, followed by a second increase. The electrical conductivity went on decreasing, which could result from the acidity decrease still observed during this stage (Fig. 2) and from the precipitation of hydrates. The thermograms of the samples aged from 5 to 18 h exhibited 4 main thermal events at ~ 60 °C, 130 170 °C (3 peaks at 130, 148 and 170 °C), 210 °C and 320 °C (Fig. 8). Their assignment was rather complex because several dehydration processes could occur within the same temperature range:

the thermal decomposition of $Ca(H_2PO_4)_2{\cdot}H_2O$ involves the dehydration of the coordinated water molecules ($Ca(H_2PO_4)_2{\cdot}H_2O \rightarrow Ca(H_2PO_4)_2 + H_2O$) in two steps (90 120 °C and 140 170 °C) and an intramolecular dehydration of the protonated phosphate groups ($Ca(H_2PO_4)_2 \rightarrow CaP_2O_6 + 2\ H_2O$) (270 300 °C) [47,48],
hydrated amorphous silica dehydrates between 45 and 100 °C and 135 150 °C [45],
as shown in stage I, the amorphous aluminum phosphate phase also dehydrates in this temperature range.

Again, the total weight loss of the sample at 7 h (9.2 ± 0.1%) was significantly higher than that calculated from the crystallized phase assemblage (~1%), which indicated that the amorphous phases contained significant amounts of water. SEM analyses carried out on the alumino phosphate amorphous phase showed that its Al/P and Zn/P molar ratios slightly decreased whereas its Ca/P ratio strongly increased from 0.16 ± 0.06 to 0.44 ± 0.03 (Fig. 6).

3.2.3. Stage 3: from 18 h to 27 h

From 18 h to 27 h, the storage modulus exhibited a third increase. It still largely exceeded the shear loss modulus (by a factor 16 at the end of the period), showing the elastic behaviour of the material. The cement paste consolidated and the Vicat end of setting was measured at 19 h. Dissolution of wollastonite accelerated (Fig. 4), as well as the formation of amorphous silica. The amount of MCPM remained approximatively constant before decreasing from 24 h. Precipitation of brushite was also noticed from this hydration time. As for the alumino phosphate amorphous phase, its amount showed little variation over the whole period, but it still continued to enrich in calcium, its Ca/P molar ratio increasing from 0.43 ± 0.03 to 0.48 ± 0.03 (Fig. 6).

During the third stage, the conductivity remained constant and the heat flow started to decrease, before exhibiting a third peak of small magnitude at 24 h. The levelling off of the electrical conductivity could be explained by the occurrence of two antagonistic processes:

1. conversion of MCPM into brushite which released H^+ and $H_2PO_4^-$ ions in solution ($Ca(H_2PO_4)_2{\cdot}H_2O + H_2O \rightarrow CaHPO_4{\cdot}2H_2O + H^+ + H_2PO_4^-$),
2. dissolution of wollastonite which continued to consume H^+ ions ($CaSiO_3 + 2H^+ \rightarrow Ca^{2+} + SiO_2 + H_2O$).

The heat flow also depended on the respective rates of reactions with opposite effects such as:

dissolution of wollastonite which was strongly exothermic (Table 2),
conversion of MCPM into brushite which was slightly endothermic (Table 2).

From 24 h to 25 h, the exothermic reactions predominated over the endothermic ones.

3.2.4. Stage 4: from 27 h to 48 h

From 27 h to 48 h, the storage modulus increased more slowly and reached 10 MPa at the end of the period (Fig. 3). MCPM was almost fully depleted after 30 h (Fig. 4). Wollastonite continued to react,

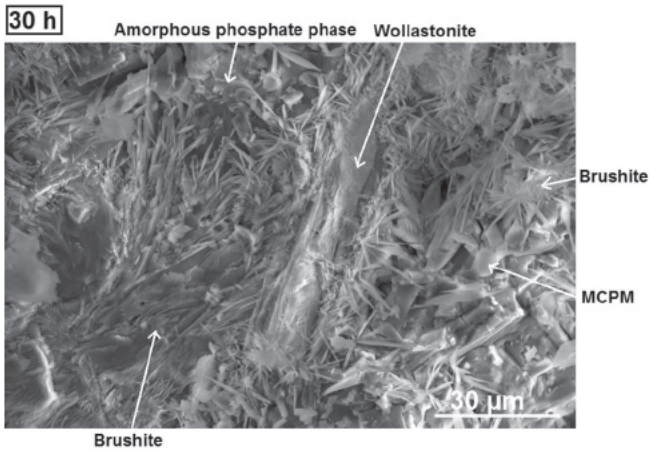

Fig. 9. SEM observation of a fracture of the cement paste aged of 30 h: (1) Brushite; (2) MCPM; (3) Wollastonite and (4) Phosphate-rich phase containing aluminum, zinc and calcium.

mainly to yield brushite and amorphous SiO_2. Elemental mapping showed that silica (in green) was present at the initial location of wollastonite grains (Fig. 10). This suggests an incongruent dissolution of wollastonite, as previously noticed in the literature [49 51]. The weakly bonded, network modifying calcium cations are released to solution relatively quickly as they exchange for hydrogen ions while the covalently bonded silicate network formers remain behind to form a hydrogen enriched leached layer that dissolves much more slowly. The amount of the amorphous alumino phosphate phase did not evolve, but its calcium content still increased slightly (Fig. 6). The electrical con ductivity dropped to a value close to zero (Fig. 3), which could result from a decrease in the acidity of the pore solution (when they are fully hydrated, brushite cement pastes exhibit a pore solution pH close to 6 [52]), but also from a loss of mobility of the ionic species in the pore solution due to the consolidation of the material. The heat production also diminished (Fig. 3) because of the slower dissolution of wollasto nite.

The microstructure of the 30 h old cement paste was observed on a fracture by scanning electron microscopy (Fig. 9): MCPM and brushite respectively crystallized as platelets and wires, while needle shaped wollastonite was still observed. The phosphate rich phase containing Al, Zn and Ca did not exhibit any characteristic morphology. The composition of this amorphous phase was again determined by Rietveld and elemental analyses of the solid phase. It was calculated as $(ZnO)_{0.39 \pm 0.06}(Al_2O_3)_{0.22 \pm 0.03}(CaO)_{0.70 \pm 0.4}(P_2O_5)\cdot yH_2O$ at 48 h. The Al/P and Zn/P ratios fitted well with those determined by EDS analysis (0.22 ± 0.01 and 0.21 ± 0.01 respectively). A deviation was still observed for the Ca/P ratio. The ratio calculated from mass balance equations (0.35 ± 0.2) was lower than that measured by EDS analysis (0.57 ± 0.02). The calculated value exhibited however a large un certainty (due to the accumulation of uncertainties on the Rietveld quantification of wollastonite, MCPM and brushite as well as on the analysis of calcium by ICP AES). Besides, the possible intermixing of the alumino phosphate phase with other calcium containing minerals (brushite and wollastonite) could not be ruled out and would lead to overestimate its calcium content.

The 48 h old paste sample was additionally characterized by ^{31}P and ^{27}Al MAS NMR spectroscopy (Fig. 7). The ^{31}P spectrum exhibited a sharp resonance peak at a chemical shift of 1.4 ppm assigned to brushite [43]. The contributions at −1.4 ppm and −4.4 ppm, previously ob served on the 30 min old sample and attributed to the alumino phos phate amorphous phase, were still noticed. Similarly, the ^{27}Al spectrum showed one main peak at a position of −10.7 ppm, which was typical of six fold coordinated aluminum forming Al $(OP)_6$ units. However, this peak was shifted as compared with that recorded on the 30 min old

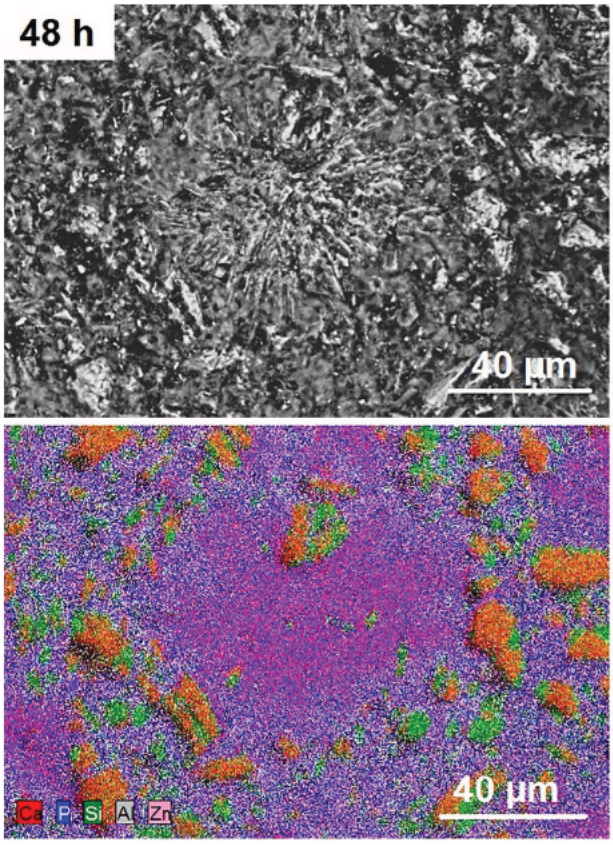

Fig. 10. SEM observation of the polished section of a 48 h-old sample. Top: BSE image; Bottom: elemental mapping (Ca, Al, P, Si, Zn).

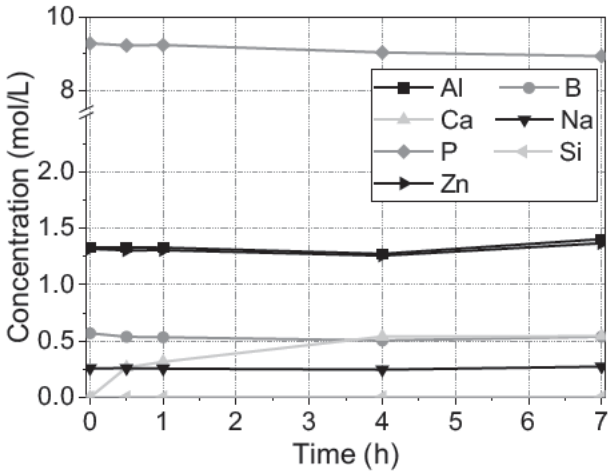

Fig. 11. Variations of the concentration of aluminum, boron, calcium, sodium, phos phorus, silicon and zinc in the liquid phase over the first 7 h of hydration.

sample (δ = −13.3 ppm). This shift of position indicated a change in the aluminum environment which might result from the higher calcium content of the alumino phosphate phase after 2 days of hydration. Be sides, the minor contributions observed on the ^{27}Al spectrum remained at the same position (7.9 and 57.9 ppm), with the same contribution (5%).

3.3. Evolution of the composition of the interstitial solution over the first 7 h

Fig. 11 plots the concentrations of Ca, P, Al, Zn, Na and B in the interstitial solution as a function of the hydration time. The Ca

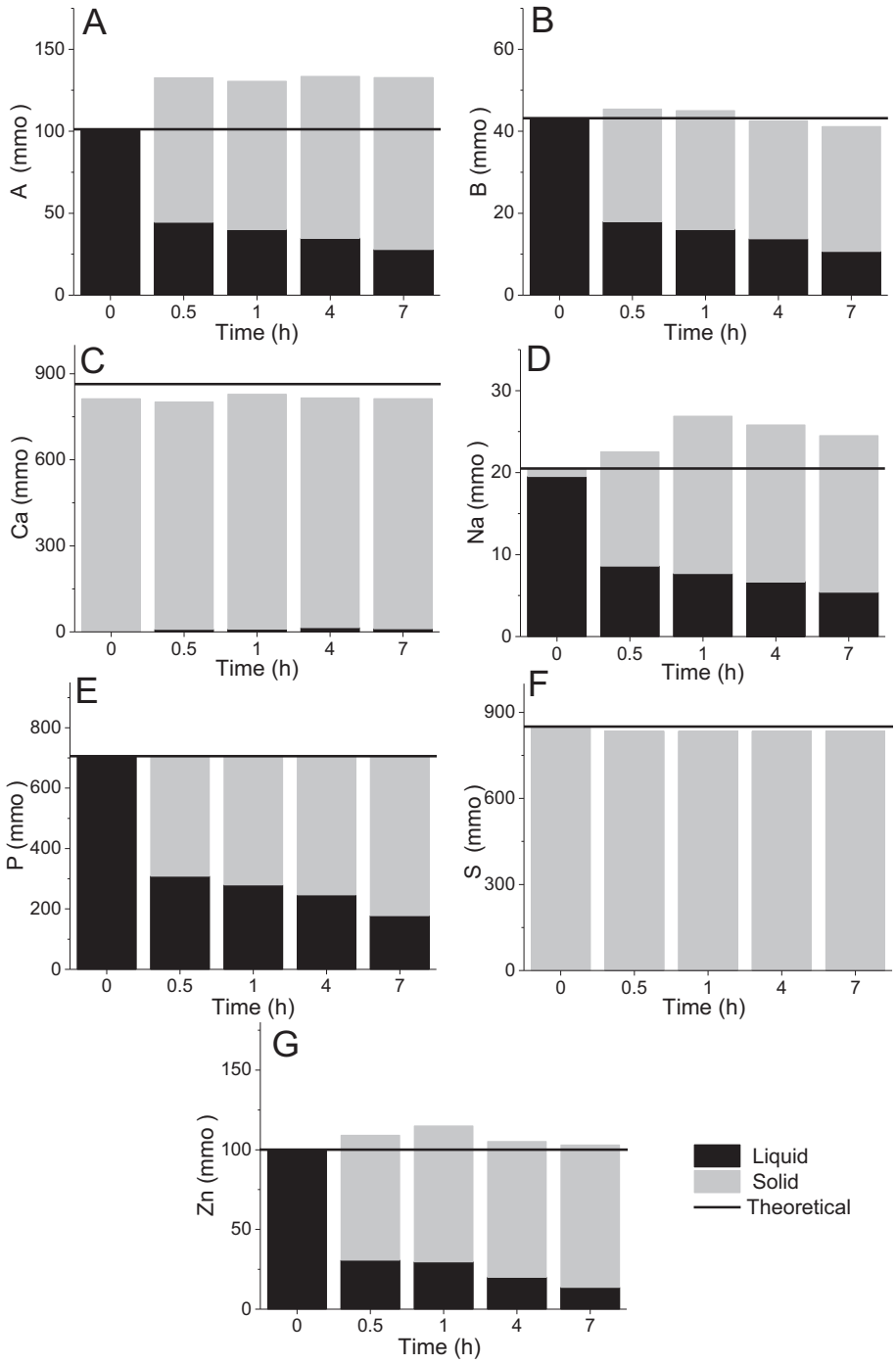

Fig. 12. Distribution of the amount of aluminum (A), boron (B), calcium (C), sodium (D), phosphorus (E), silicon (F) and zinc (G) between the liquid and solid phases over the first 7 h of hydration.

concentration, resulting from the dissolution of wollastonite, increased over time while the P concentration decreased due to the precipitation of phosphate containing hydrates. The Si concentration was very low in solution (below 2 mmol/L) at each hydration time. The Na and B con centrations remained almost constant (0.26 and 0.52 mol/L respec tively) and were governed by the solubility of borax $Na_2B_4O_7$ (0.128 mol/L at 20 °C [53]). Similarly, the Al and Zn concentrations showed little variation over time. However, since the hydration process consumed some water, their amount in solution should tend to de crease. This was checked by calculating the mol numbers of the dif ferent elements in solution. The volume of liquid phase was assessed using Eq.12, with V the volume of solution, $n_P^{initial}$ and n_P^{solid} the amounts of phosphate initially in the solution and in the solid at time t respectively and $[P]_{liquid}$ the phosphate concentration in solution at time t.

$$V = \frac{n_P^{initial} - n_P^{solid}}{[P]_{liquid}} \quad (12)$$

Fig. 12 shows their distribution in the liquid and solid phases with ongoing hydration. A significant fraction of Al and Zn was actually insolubilized from the first characterization time, which was consistent with the precipitation of the amorphous phosphate phase containing zinc and aluminum observed experimentally. For each element, the total of its dissolved (determined from the analysis of the liquid phase) and precipitated amounts (determined from the analysis of the solid phase) was in acceptable agreement with that introduced initially given the analytical uncertainties.

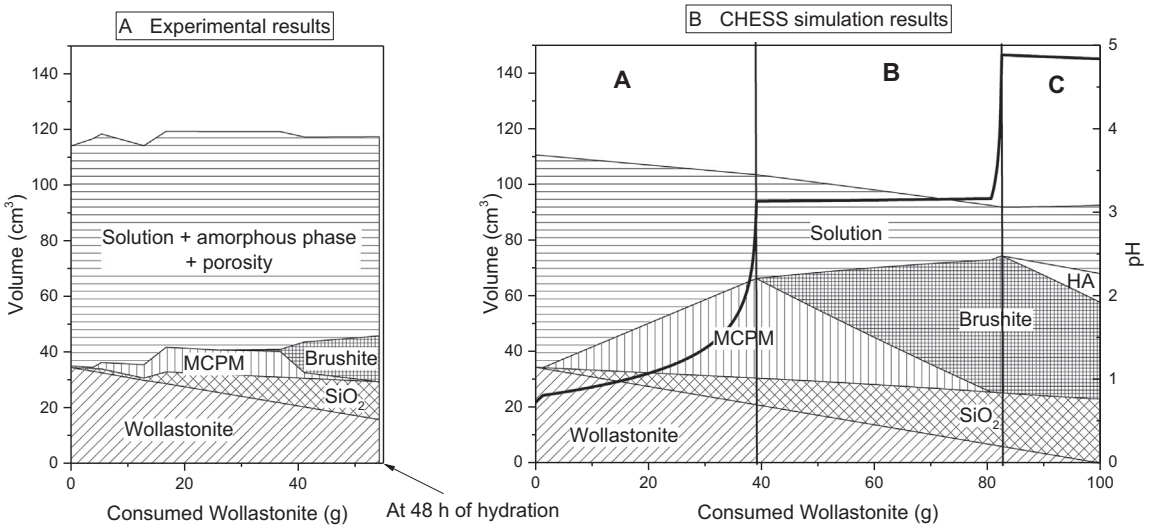

Fig. 13. Volume and phase evolution during the hydration of wollastonite by a phosphoric acid solution A- Experimental results, B- Modelling results.

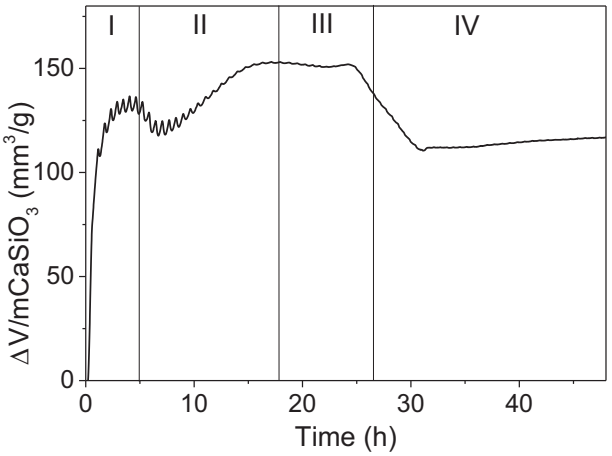

Fig. 14. Measured volume variation during hydration of wollastonite.

3.4. Modelling of wollastonite reaction

Thermodynamic modelling of the phase development was investigated for a simplified system comprising 100 g of wollastonite and 76 mL of a 9 mol/L H_3PO_4 solution with 0.15 mol/L $Na_2B_4O_7$. The Ca/P, B/P, Na/P molar ratios and the liquid/solid weight ratio were the same as in the cement paste investigated experimentally. In this first modelling approach, the zinc and aluminum cations were omitted because of the lack of thermodynamic data concerning their reaction product (amorphous phosphate phase). With the densities of all phases present (Table 3), the evolution of the individual phase volumes was calculated as a function of the amount of consumed wollastonite and compared to the experiment (Fig. 13). The simulation showed three main steps in the hydration process of wollastonite.

Step A (depleted wollastonite ranging from 0 to 39%): the pH increased by more than two units; MCPM, which is known to be stable in acidic medium [52], precipitated, as well as amorphous silica.
Step B (depleted wollastonite ranging from 39% to 82%): the pH reached a plateau at 3.1; MCPM dissolved and brushite precipitated. The dissolution of MCPM was governed by the pH increase: MCPM is unstable at pH above 2, while brushite is stable at pH values between 2 and 6 [52]. At the end of this stage, the pH increased again by 1 unit.
Step C (depleted wollastonite ranging from 82 to 100%): the pH increased again by one unit, causing the dissolution of a small fraction of brushite and the precipitation of hydroxyapatite (HA), the most insoluble calcium phosphate phase in slightly acidic, neutral or basic medium.

This simulation reproduced the precipitation sequence observed experimentally: $CaSiO_3 + H_3PO_4 \rightarrow SiO_2(am) + MCPM \rightarrow SiO_2(am)$ + Brushite. The transient precipitation of MCPM was therefore governed by thermodynamic considerations: MCPM was the most stable calcium phosphate at the beginning of hydration when the pH was low. Then, the pH increase led to the destabilization of MCPM and precipitation of brushite. The precipitation of hydroxyapatite was not observed experimentally since wollastonite had not completely reacted: at the end of the experiment (48 h), about 40 wt% of wollastonite remained in the paste sample. Another difference was the amount of MCPM and brushite which precipitated: it was overestimated by the simulation, as compared with the experiment. This resulted from the fact that the precipitation of the alumino phosphate phase containing some calcium was neglected in the calculation.

The simulation predicted an increase in the volume of solids and a decrease in the volume of liquid (more important when brushite formed instead of MCPM) which resulted in a net decrease in the total volume (18 cm^3/100 g of wollastonite for complete reactions). The apparent volume variation of the cement paste was measured experimentally using the shrinkage cone device (Fig. 14). The results showed that the volume of paste increased during the first period of hydration, which mainly resulted from the decarbonation of calcite (present in small amount in the cement powder) in acidic medium (Eq. (13)). The gas production created porosity.

$$CaCO_3 + 2H^+ \rightarrow Ca^{2+} + CO_2 + H_2O \quad (13)$$

Then, the volume increased as MCPM precipitated. Finally the conversion of MCPM into brushite caused a shrinkage (Fig. 14), which was consistent with the trend expected from thermodynamic calculations (Fig. 13 B). At the end of experiment, the apparent volume exhibited a net increase by 5% as compared to the initial volume, corresponding to 10 cm^3/100 g of wollastonite.

4. Conclusion

This work, focused on the hydration of wollastonite by an orthophosphoric solution in the presence of borax and metallic cations (Al^{3+}, Zn^{2+}), led to the following conclusions.

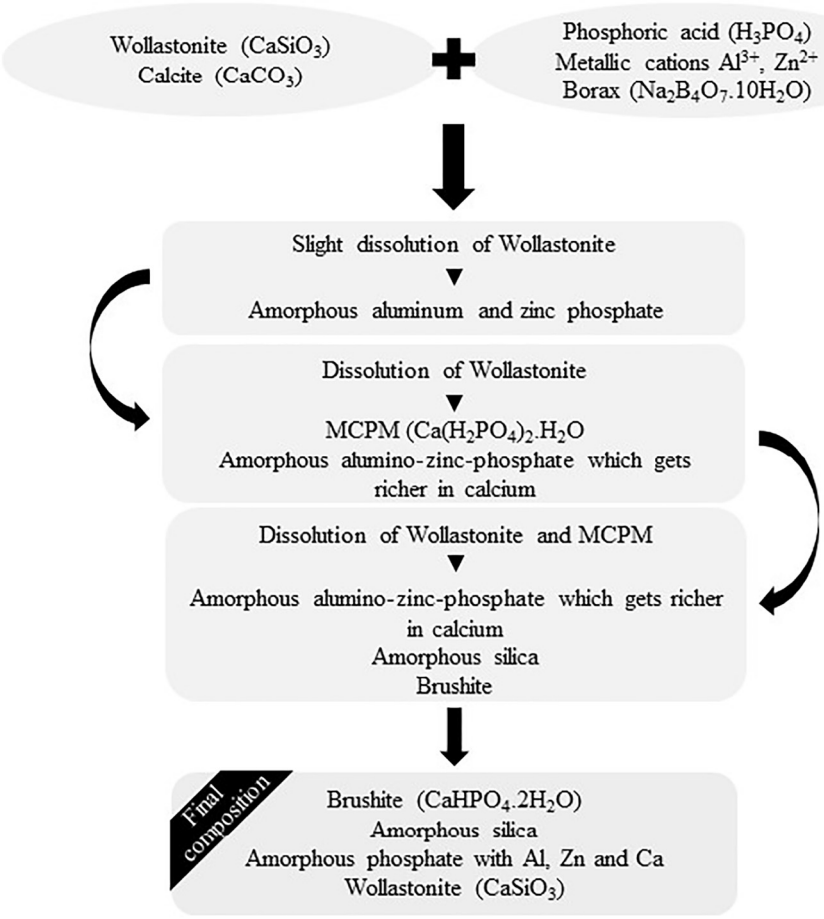

Fig. 15. Summary of the hydration process of wollastonite with a solution of phosphoric acid containing aluminum, zinc and borax.

Table 3
Density and molar volume of phases used for thermodynamic calculations [4].

Phase	Formula	Density (g/cm^3)	Molar volume (cm^3/mol)
Wollastonite	$CaSiO_3$	2.909	39.88
Brushite	$CaHPO_4{\cdot}2H_2O$	2.32	74.13
Silica	SiO_2	2.072	28.96
MCPM	$Ca(H_2PO_4)_2{\cdot}H_2O$	2.23	113.00
Hydroxyapatite	$Ca_5(PO_4)_3(OH)$	3.15	159.36

1. Hydration is a multi step process summarized in Fig. 15. Amorphous silica is formed by incongruent dissolution of wollastonite. In addition, several phosphate products precipitate

   an amorphous phase containing Al, Zn and Ca which massively forms during the first minutes after mixing, and which progressively becomes richer in calcium as hydration progresses,
   monocalcium phosphate monohydrate ($Ca(H_2PO_4)_2{\cdot}H_2O$ MCPM), which forms transiently,
   brushite ($Ca(HPO_4){\cdot}2H_2O$), which forms once MCPM starts to destabilize.

2. The evolution of the phase assemblage is partially described by thermodynamic modelling. The conversion of MCPM into brushite is governed by the pH evolution: the former is stable at pH below 3, the latter at higher pH. The model should be improved however by taking into account the amorphous phosphate phase which was neglected in this preliminary approach.
3. Consolidation of the cement paste occurs in three main stages. Its storage modulus exhibits a first increase of small magnitude just after mixing, when the amorphous phosphate phase precipitates. Its second and third increases are correlated with the massive precipitation of MCPM and brushite respectively. The Vicat setting occurs once brushite starts to precipitate.

Future work should investigate the long term evolution of the paste samples depending on their curing conditions and the influence of the formulation parameters on the hydration process, such as the Ca/P ratio and the initial concentrations of aluminum, zinc and borax in the solution.

Acknowledgements

Acknowledgements are due to Pascal Antonucci for his help in the laboratory as well as Julien Aupoil and Jean Baptiste Champenois for their help on the acidity function.

References

[1] L.C. Chow, Development of self-setting calcium phosphate cement, The Centennial Memorial Issue of The Ceramic Society of Japan 99 (1991) 954–964.
[2] I. Older, Special Inorganics Cements, Taylor & Francis Group, New York, 2000.
[3] A. Wagh, Calcium phosphate cements, in: E. Hurtz (Ed.), Chemically Bonded Phosphate Ceramics: twenty first Century Materials With Diverse Applications, Elsevier Science Ltd., Oxford, 2004, pp. 143–156.
[4] C. Janot, B. Ilschner, Biocéramiques et biociments résorbables pour le comblement osseux, in: Traité des matériaux: Matériaux émergents, Presses polytechniques et universitaires Romanes, 2001.
[5] C. Rey, M. Frèche, M. Heughebaert, J.C. Heughebaert, J.L. Lacout, A. Lebugle, J. Szilagyi, M. Vignoles, Apatite chemistry in biomaterial preparation, shaping and biological behaviour, Bioceramics, Butterworth-Heinemann, 1991, pp. 57–64.
[6] F.C.M. Driessens, M.G. Boltong, O. Bermudez, J.A. Planell, Formulation and setting times of some calcium orthophosphate cements: a pilot study, J. Mater. Sci. Mater. Med. 4 (1993) 503–508.
[7] T.W. Song, H.Y. Kim, Synthesis and properties of self-hardening calcium phosphate

cements for biological application, J. Korean Ceram. Soc. 3 (1997) 129–133.
[8] M.P. Ginebra, M. Espanol, E.B. Montufar, R.A. Perez, G. Mestres, New processing approaches in calcium phosphate cements and their applications in regenerative medicine, Acta Biomater. 6 (2010) 2863–2873.
[9] C. Canal, M.P. Ginebra, Fibre-reinforced calcium phosphate cements: a review, J. Mech. Behav. Biomed. Mater. 4 (2011) 1658–1671.
[10] G. Cama, 1 - Calcium phosphate cements for bone regeneration, Biomaterials for Bone Regeneration, Woodhead Publishing, 2014, pp. 3–25.
[11] J. Zhang, W. Liu, V. Schnitzler, F. Tancret, J.-M. Bouler, Calcium phosphate cements for bone substitution: Chemistry, handling and mechanical properties, Acta Biomater. 10 (2014) 1035–1049.
[12] J.C. Elliott, Structure and chemistry of the apatites and other calcium orthophosphates, Elsevier, Amsterdam, 1994 (389 pp).
[13] C.E. Semler, Lime Silico Phosphate Ceramics, The United States Department of Transportation, Washington DC, USA, 1974, p. 6 3,804,661.
[14] C.E. Semler, A quick-setting wollastonite phosphate cement, Ceramics Bulletin 55 (1976) 983–988.
[15] G. Mosselmans, M. Biesemans, R. Willem, J. Wastiels, M. Leermakers, H. Rahier, S. Brughmans, B. Van Mele, Thermal hardening and structure of a phosphorus containing cementitious model material, J. Therm. Anal. Calorim. 88 (2007) 723–729.
[16] A.D. Wilson, J.W. Nichloson, Acid-base cements: Their biomedical and insdustrial applications, Cambridge University Press, Cambridge, 1993.
[17] M. Alshaaer, H. Cuypers, H. Rahier, J. Wastiels, Production of monetite-based Inorganic Phosphate Cement (M-IPC) using hydrothermal post curing (HTPC), Cem. Concr. Res. 41 (2011) 30–37.
[18] X. Wu, J. Gu, Inorganic Resins Composition, Their Preparation and use Thereof, Vrije Universiteit, Brussel, Belgium, 2000, p. 15 EP 0861216 B1.
[19] H.A. Colorado, J. Pleitt, C. Hiel, J.M. Yang, H.T. Hahn, C.H. Castano, Wollastonite based-Chemically Bonded Phosphate Ceramics with lead oxide contents under gamma irradiation, J. Nucl. Mater. 425 (2012) 197–204.
[20] H.A. Colorado, C. Hiel, T. Hahn, J.M. Yang, Wollastonite based chemically bonded phosphate ceramics composites, in: J. Cuppoletti (Ed.), Metal, Ceramic and Polymeric Composites for Various Uses, InTech, Croatia, 2011.
[21] H.A. Colorado, Z. Wang, J.-M. Yang, Inorganic phosphate cement fabricated with wollastonite, barium titanate, and phosphoric acid, Cem. Concr. Compos. 62 (2015) 13–21.
[22] M. Alshaaer, H. Cuypers, G. Mosselmans, H. Rahier, J. Wastiels, Evaluation of a low temperature hardening Inorganic Phosphate Cement for high-temperature applications, Cem. Concr. Res. 41 (2011) 38–45.
[23] J.-B. Champenois, C. Cau Dit Coumes, A. Poulesquen, P. Le Bescop, D. Damidot, Beneficial use of a cell coupling rheometry, conductimetry, and calorimetry to investigate the early age hydration of calcium sulfoaluminate cement, Rheol. Acta 52 (2013) 177–187.
[24] M. Choplin, P. Marchal, Sytemic rheology or how to extend the process viscosity concept, in: 12th International Congress of Rheology, Quebec, Can. Underwrit. (1996) 665–666.
[25] A. Aït-Kadi, P. Marchal, L. Choplin, A.-S. Chrissemant, M. Bousmina, Quantitative analysis of mixer-type rheometers using the Couette analogy, Can. J. Chem. Eng. 80 (2002) 1166–1174.
[26] J. Kaufmann, F. Winnefeld, D. Hesselbarth, Effect of the addition of ultrafine cement and short fibber reinforcement on shrinkage, rheological and mechanical properties of Portland cement pastes, Cem. Concr. Compos. 26 (2004) 541–549.
[27] S. Eppers, C. Müller, The shrinkage cone method for measuring the autogenous shrinkage - an alternative to the corrugated tube method, International RILEM Conference on Use of Superabsorbent Polymers and Other New Additives in Concrete, Technical University of Denmark, Lyngby, Denmark, 2010, pp. 67–76.
[28] E. Lafond, C. Cau Dit Coumes, S. Gauffinet, D. Chartier, P. Le Bescop, L. Stefan, A. Nonat, Investigation of the swelling behavior of cationic exchange resins saturated with Na + ions in a C3S paste, Cem. Concr. Res. 69 (2015) 61–71.
[29] C. Frontera, J. Rodriguez-Carvajal, FullProf as a nex tool for flipping ratio analysis, Physica B 335 (2003) 219–222.
[30] L.P. Hammett, The theory of acidity, J. Am. Chem. Soc. 50 (1928) 2666–2673.
[31] K.L. Elmore, C.M. Mason, J.H. Christensen, Activity of orthophosphoric acid in aqueous solution at 25 °C from vapor pressure measurments, J. Am. Chem. Soc. 68 (1946) 2528–2532.
[32] C. Louis, J. Bessière, Étude physico-chimique des solutions concentrées en acide phosphorique par voie électrochimique. Propriétés acido-basiques et oxydo-réductrices, Can. J. Chem. 63 (1984).
[33] M.I. Vinnick, Acidity functions of aqueous solutions of strong acids, Russ. Chem. Rev. 35 (1966) 802–817.
[34] M.A. Paul, F.A. Long, H0 and related indicator acidity function, Chem. Rev. 57 (1957) 1–47.
[35] E.M. Arnett, G.W. Mach, Solvent effects in organic chemistry. VIII. Acidity function failure in different aqueous acids, J. Am. Chem. Soc. 88 (1966) 1177–1183.
[36] D.G. Lee, R. Stewart, H0 acidity functions for nitric and phosphoric acid solutions containing added sodium perchlorate, Can. J. Chem. 42 (1964) 486–489.
[37] E. Heibronner, S. Weber, Die Hammett'sche Säurefunktion des Systems Phosphorsäure/Wasser, Helv. Chim. Acta 32 (1949) 1513–1517.
[38] J. Van der Lee, Thermodynamic and Mathematical Concepts of CHESS, T. R. LHM/RD/98/39, (1998).
[39] D. Damidot, B. Lothenbach, D. Herfort, F.P. Glasser, Thermodynamics and cement science, Cem. Concr. Res. 41 (2011) 679–695.
[40] M. Cherif, A. Mgaidi, N. Ammar, G. Vallée, W. Fürst, A new investigation of aqueous orthophosphoric acid speciation using Raman spectroscopy, J. Solut. Chem. 29 (2000).
[41] H.C. Helgeson, Thermodynamics of complex formation in aqueous solution at elevated temperatures and pressures, Am. J. Sci. (1967) 729–804.
[42] M. Jabri, E. Mejdoubi, M. El Gadi, B. Hammouti, Optimisation of hardness and setting time of dental zinc phosphate cementusing a design of experiments, Arab. J. Chem. 5 (2012) 347–351.
[43] A.P. Legrand, H. Sfihi, N. Lequeux, J. Lemaitre, (31) P Solid-State NMR study of the chemical setting process of a dual-paste injectable brushite cements, J Biomed Mater Res B Appl Biomater 91 (2009) 46–54.
[44] K. MacKenzie, M.E. Smith, Multinuclear Solid-state Nuclear Magnetic Resonance of Inorganic Materials, 1 ed., Pergamon, 2002.
[45] E. Huseynov, Thermogravimetric and differential thermal analysis of nano SiO_2 - H_2O systems, The Journal of the International Association of Physics Students (2013) (Jul. 5, 2013).
[46] S. Cerveny, G. Schwartz, J. Otegui, J. Colmenero, J. Loichen, S. Westermann, Dielectric study of hydration water in silica nanoparticles, J. Phys. Chem. C 116 (2012) 24340–24349.
[47] A. Ioițescu, G. Vlase, T. Vlase, N. Doca, Kinetics of decomposition of different acid calcium phosphates, J. Therm. Anal. Calorim. 88 (2007) 121–125.
[48] B. Boonchom, Parallelogram-like microparticles of calcium dihydrogen phosphate monohydrate ($Ca(H_2PO_4)2{\cdot}H_2O$) obtained by a rapid precipitation route in aqueous and acetone media, J. Alloys Compd. 482 (2009) 199–202.
[49] W.H. Casey, B. Bunker, Leaching of mineral and glass surfaces during dissolution, in: M.F. Hochella, A.F. White (Eds.), Mineral-Water Interface Geochemistry, Mineralogical Society of America, 1990, pp. 397–426.
[50] E.J. Weisshart, J.D. Rimstidt, Wollastonite: incongruent dissolution and leached layer formation, Geochim. Cosmochim. Acta 64 (2000) 4007–4016.
[51] E. Green, A. Luttge, Incongruent dissolution of wollastonite measured with vertical scanning interferometry, Am. Mineral. 91 (2006) 430–434.
[52] S.V. Dorozhkin, Calcium Orthophosphate Cements and Concretes, Dent. Mater. 2 (2009) 221–291.
[53] Lange's Handbook of Chemistry, 15 ed., (1999).
[54] P. Vieillard, Y. Tardy, Thermochemical Properties of Phosphates, (1984), pp. 171–198.
[55] H.C. Helgeson, J.M. Delany, H.W. Nesbitt, D.K. Bird, Summary and critique of the thermodynamic properties of rock forming minerals, Amer. J. Sci. 278A (1978) 1–229.